



Saturation transfer (CEST and MT) MRI for characterization of U-87 MG glioma in the rat

Wilfred W. Lam¹  | Agata Chudzik² | Natalia Lehman² | Artur Łazorczyk³ |
Paulina Koziół³ | Anna Niedziątek³ | Athavan Gananathan¹ |
Anna Orzyłowska²  | Radosław Rola² | Greg J. Stanisz^{1,2,4}

¹Physical Sciences Platform, Sunnybrook Research Institute, Toronto, Ontario, Canada

²Department of Neurosurgery and Paediatric Neurosurgery, Medical University of Lublin, Lublin, Poland

³Department of Radiography, Medical University of Lublin, Lublin, Poland

⁴Department of Medical Biophysics, University of Toronto, Toronto, Ontario, Canada

Correspondence

Wilfred Lam, DPhil, Sunnybrook Research Institute, 2075 Bayview Ave., Room S6 05, Toronto, Ontario, M4N 3M5, Canada.
Email: lamw@sri.utoronto.ca

Funding information

Terry Fox Research Institute, Grant/Award Number: 1115-03; Canadian Cancer Society, Grant/Award Number: 705083; Medical University of Lublin, Grant/Award Numbers: PBmd230, DS316

Abstract

The focus of this work was to identify the optimal magnetic resonance imaging (MRI) contrast between orthotopic U-87 MG tumours and normal appearing brain with the eventual goal of treatment response monitoring. U-87 MG human glioblastoma cells were injected into the brain of RNU nude rats ($n = 9$). The rats were imaged at 7 T at three timepoints for all animals: 3–5, 7–9, and 11–13 days after implantation. Whole-brain T_1 -weighted (before and after gadolinium contrast agent injection), diffusion, and fluid-attenuated inversion recovery scans were performed. In addition, single-slice saturation-transfer-weighted chemical exchange saturation transfer (CEST), magnetization transfer (MT), and water saturation shift referencing (WASSR) contrast Z -spectra and T_1 and T_2 maps were also acquired. The MT and WASSR Z -spectra and T_1 map were fitted to a two-pool quantitative MT model to estimate the T_2 of the free and macromolecular-bound water molecules, the relative macromolecular pool size ($M_{0, MT}$), and the magnetization exchange rate from the macromolecular pool to the free pool (R_{MT}). The T_1 -corrected apparent exchange-dependent relaxation (AREX) metric to isolate the CEST contributions was also calculated. The lesion on $M_{0, MT}$ and AREX maps with a B_1 of 2 μ T best matched the hyperintensity on the post-contrast T_1 -weighted image. There was also good separation in Z -spectra between the lesion and contralateral cortex in the 2- μ T CEST and 3- and 5- μ T MT Z -spectra at all time points. A pairwise Wilcoxon signed-rank tests with Holm–Bonferroni adjustment on MRI parameters was performed and the differences between enhancing lesion and contralateral cortex for the MT ratio with 2 μ T saturation at 3.6 ppm frequency offset (corresponding to the amide chemical group) and $M_{0, MT}$ were both strongly significant ($p < 0.001$) at all time points. This work has

Abbreviations: AREX, apparent exchange-dependent relaxation; CEST, chemical exchange saturation transfer; CPMG, Carr–Purcell–Meiboom–Gill; FLAIR, fluid-attenuated inversion recovery; IR, inversion recovery; $M_{0, MT}$, relative MT macromolecular pool size; MT, magnetization transfer effect from semisolid macromolecules; MTR, magnetization transfer ratio; MTR_{ASYM} , magnetization transfer ratio asymmetry; RARE, rapid acquisition with relaxation enhancement; R_{MT} , magnetization exchange rate from the macromolecular to free water pools; rNOE, relayed nuclear Overhauser effect; $T_{1, obs}$, observed longitudinal relaxation time; $T_1W + C$, post-contrast agent injection T_1 -weighted image; T_2, F , transverse relaxation time of the free water pool; $T_{2, obs}$, observed transverse relaxation time; $T_{2, MT}$, transverse relaxation time of the macromolecular water pool.

Wilfred W. Lam and Agata Chudzik contributed equally to this work.

This is an open access article under the terms of the [Creative Commons Attribution-NonCommercial](https://creativecommons.org/licenses/by-nc/4.0/) License, which permits use, distribution and reproduction in any medium, provided the original work is properly cited and is not used for commercial purposes.

© 2024 The Author(s). *NMR in Biomedicine* published by John Wiley & Sons Ltd.

identified that differences between enhancing lesion and contralateral cortex are strongest in MTR with $B_1 = 2 \mu\text{T}$ at 3.6 ppm and relative macromolecular pool size ($M_{0, \text{MT}}$) images over entire period of 3–13 days after cancer cell implantation.

KEYWORDS

brain tumour, chemical exchange saturation transfer, diffusion, glioblastoma, glioma, magnetization transfer

1 | INTRODUCTION

Gliomas are among the most common brain tumours in the adult central nervous system and present a significant burden on the health system: the combination of surgery, chemotherapy, and radiation for glioblastoma treatment had a mean cost (studied from 2006 to 2013) of \$62,602.¹ The 2-year overall survival rate is only 6.7%, the quality of life in all domains is very poor,² and its incidence is on the rise (with a six-fold increase over 10 years between 2008 and 2017³). There is a need for more precise stratification of gliomas by developing noncontrast-agent-based and quantitative magnetic resonance imaging (MRI) techniques that can help monitor response during the treatment. Identifying specific cohorts based on molecular stratification and imaging response helps devise better strategies for combinatorial treatments including molecularly selective therapies.

High-grade glioma treatment response assessment, commonly using standardized MRI,⁴ has been an area of active research.^{5–9} Following cytoreductive surgery and radiotherapy with concomitant and adjuvant temozolomide chemotherapy,^{10,11} the lesion can exhibit true tumour progression (TP), pseudoprogression (PsP), or both. Stereotactic biopsy in 50 patients has found TP in 60%, PsP in 6%, and a mixture in 34%.¹² TP has poorer prognosis than PsP.¹³

Clinically, the highest of discrimination between TP and PsP comes with magnetic resonance (MR) spectroscopy (generally a non-imaging technique) with a sensitivity/specificity of 91%/95%¹⁴ compared to those of the imaging techniques diffusion-weighted MRI (DWI) with 71%–90%/82%–87%, dynamic contrast enhanced MR with 87%–88%/86%–88%, and dynamic susceptibility contrast MR with 88%–92%/77%–85%^{14,15}; the range of values reflects differences in the meta-analyses cited. The diagnostic accuracies of other advanced techniques, for example, arterial spin labelling MR, amide proton transfer weighted (APT_w) MR, and O-(2-[¹⁸F]fluoroethyl)-L-tyrosine (¹⁸F-FET) positron emission tomography (PET), are largely unknown due to low numbers of studies in literature.¹⁵

Novel treatment response biomarkers include PET tracers,¹⁶ combined MR/PET tracers,¹⁷ dynamic contrast enhancement,¹⁸ dynamic susceptibility contrast,¹⁹ and the use of iron oxide nanoparticle MRI tracers.²⁰ General glioma characterization has also been undertaken with T_2 -weighted imaging²¹ and manganese-based contrast agents,²² modified gadolinium (Gd) contrast agents,²³ oxygen-enhanced MRI,²⁴ hypoxia, and vascular endothelial growth factor expression with T_2^* -weighted imaging,²⁵ perfusion with arterial spin labeling,²⁶ angiogenesis with lipoCEST,²⁷ DWI,²⁸ and relaxometry.²⁸

Saturation transfer MRI (ST-MRI) is one of the relatively new MR contrast mechanisms where use in brain cancer MRI stratification and evaluation of treatment has been constantly growing.^{29–31} Major subtypes of ST-MRI include magnetization transfer (MT) and chemical exchange saturation transfer (CEST) contrast. MT is sensitive to semisolid macromolecules, such as lipids in cell membranes and myelin.³² CEST and the related relayed nuclear Overhauser effect (rNOE) are sensitive to specific chemical groups (e.g., amide, guanidinium, and aliphatic) in dissolved proteins.^{33,34} Preclinically, saturation transfer MR has also been investigated in rat glioma models.^{35–39} Clinically, ST-MRI has been shown to discriminate between clinical treatment responders and non-responders immediately after the end of chemoradiotherapy.^{40–42}

Clinically, ST-MRI has been found to be promising in differentiating TP from PsP, tumour grading, and treatment response prediction. Jiang et al.⁴³ have found that APT_w differentiates TP from PsP (area under the receiver operating characteristic curve [AUC]: 0.881) in recurrent malignant glioma ($n = 21$) at 3 T, which has been validated with histopathology. Similarly, Park et al.⁴⁴ report that, compared with conventional T_1 -weighted post-contrast imaging alone, the addition of APT significantly improves AUC from 0.58–0.74 to 0.89–0.91 in glioblastoma ($n = 65$). Choi et al.⁴⁵ have investigated the use of APT to distinguish between low- and high-grade gliomas, also at 3 T, and report that using both the APT signal and apparent diffusion coefficient (ADC) significantly improves discrimination vs the ADC alone (AUC: 0.888 vs 0.910) in adult diffusion glioma ($n = 46$). Regnery et al.⁴⁶ have found that the NOE signal isolated using Lorentzian difference (a CEST- and MT-derived metric) could be used to predict early glioblastoma progression (AUC: 0.98) before treatment at 7 T ($n = 20$).

Preclinical work in animal models of glioma is important because it provides validation of imaging methods via histopathology⁴⁷ and allows for testing novel therapeutics. In addition to quantifying tumour characteristics, which can potentially be applied to clinical settings, imaging can be done more frequently than would be possible with a patient population to detect quick changes. That is why the U-87 MG rat glioblastoma model was used in the present work to investigate the utility of CEST and MT contrast which in this case did not require exogenous contrast agent, to evaluate tumour growth.

2 | METHODS

2.1 | Tumour implantation

U-87 MG human glioblastoma cells⁴⁸ (Cell Line Service, Eppelheim, Germany) were cultured in RPMI 1640 medium (Gibco, Grand Island, NY) containing 10% foetal bovine serum (PAN-Biotech, Aidenbach, Germany) and 1% penicillin–streptomycin solution 100X (Euroclone, Pero, Italy). U-87 MG cells were harvested by trypsinization, washed twice with RPMI 1640 medium, and resuspended in RPMI. Stereotaxic injections were prepared as described previously.⁴⁹ Briefly, a cell suspension containing $(3-5) \times 10^5$ cells per 6 μL of RPMI was used for implantation into the right striatum of nine male RNU nude rats (weight: 180–220 g; Charles River, Sulzfeld, Germany). Rats were placed in a stereotaxic apparatus (Neurostar, Tübingen, Germany) with StereoDrive software (v6.6.3) with integrated Paxinos rat brain atlas. They were kept under isoflurane/oxygen anaesthesia (3.5% for induction and 2%–2.5% for maintenance). Following a midline scalp incision, a burr hole was placed in the skull at 0.5 mm anterior and 3 mm lateral from the bregma. Using a 10- μL Hamilton syringe, 3 μL of cell suspension was injected at a depth of 4.5 mm from the brain surface, and another 3 μL was injected at a depth of 4 mm. Each injection took approximately 5 min. The syringe was left in place each time for at least 2 min before retraction to prevent reflux of the injected material. The animals' weight and well-being were assessed every other day.

All experimental procedures were approved by the Local Ethical Committee for Animal Experiments, University of Life Sciences in Lublin based on Polish law Dz. U. 2015 poz. 266, art. 48, pkt. 1.

2.2 | MRI acquisition

The rats were scanned at 7 T (PharmaScan 70/16 US; Bruker BioSpin, Ettlingen, Germany) running ParaVision (v6.0.1) with a 72-mm inner diameter volume transmit coil and 20-mm loop receive coil. The rats were anesthetized using a blend of isoflurane and oxygen with 3.5% for induction and 1.7%–2.5% for maintenance. A tail vein catheter was placed for gadolinium administration. Respiratory rate and temperature were continuously observed using an MR-compatible Small Animal Monitoring System (SA Instruments, Stony Brook, NY). The animals were allowed to breathe freely during the MR scan and the anaesthesia level was regulated to keep their respiratory rate around 50 breaths/min. Additionally, their body temperature was maintained at 37°C by circulating water. Imaging was performed at three timepoints for all animals: 3–5, 7–9, and 11–13 days after implantation. A whole-brain, structural T_1 -weighted (T_{1w}) fast low angle shot⁵⁰ (FLASH; 12 min 50 s) scan was followed by T_2 -weighted fluid-attenuated inversion recovery⁵¹ (FLAIR; 8 min 27 s), both with 0.2 mm isotropic resolution. Shimming was performed using the scanner's *Mapshim* function. In addition, five single-slice saturation transfer rapid acquisition with refocused echoes⁵² (RARE) Z-spectra (two CEST with saturation amplitude B_1 of 0.5 and 2 μT , each 23 min 20 s; two MT with B_1 of 3 and 5 μT , each 5 min 40 s; and WATER Saturation Shift Referencing⁵³ (WASSR) with a B_1 of 0.1 μT , 8 min 20 s; all used a 4.9-s block saturation pulse). To estimate the longitudinal relaxation time T_1 , five single-slice inversion recovery (IR) RARE scans were also acquired (each 2 min). The transverse relaxation time T_2 was estimated using a single-slice Carr–Purcell–Meiboom–Gill^{54,55} (CPMG) sequence (4 min 16 s). The Z-spectra, IR RARE, and CPMG scans had 0.47 mm in-plane resolution and 1 mm slice thickness. Whole-brain DWI^{56,57} was also performed (9 min 20 s) with 0.4 mm isotropic resolution. After CEST and microstructural MRI rat were injected with gadolinium (Gd)-based contrast agent (Omniscan; GE Healthcare, Amersham, UK; 0.6 mmol/kg, corresponding to 0.1 mmol/kg in humans after adjusting for body surface area according to FDA guidance⁵⁸) and a post-Gd, 3D whole brain image ($T_{1w} + C$) was started immediately after contrast injection (using the same parameters as the T_{1w} scan); the centre of k -space was acquired approximately 6.5 min after the injection. The total acquisition time including scout and shimming was ~ 3 h per animal. An imaging protocol summary is given in Supplementary Table S1 and saturation transfer and diffusion pulse sequence details in Supplementary Tables S2 and S3, respectively.

2.3 | MRI data pre-processing

All images were converted from Bruker to *NIFTI* format using *brkraw*⁵⁹ (v0.3.7). For each animal, FLAIR and $T_{1w} + C$ images were registered rigidly to the T_{1w} image using FSL FLIRT.^{60,61} Likewise, the IR images with $\text{TI} \in \{230, 650, 800, 5000\}$ ms were registered to that with $\text{TI} = 30$ ms. Then, the T_{1w} and IR images with $\text{TI} = 30$ ms were registered to the first image in the Z-spectrum acquired with $B_1 = 2 \mu\text{T}$ and the respective transformation matrices applied to the other structural and IR images. The images with a frequency offset (i.e., the Z-spectra) or time (i.e., the CPMG scan) dimension were registered using the MATLAB's *imregister* function. In order to avoid misregistration of low SNR images (e.g., those acquired with saturation near the water resonance in a Z-spectrum), images with a magnitude less than 50% of the mean signal of the reference scan were registered using the transformation matrix of the last image with sufficient SNR (e.g., an interleaved reference scan in a Z-spectrum). A B_0 map was estimated from the WASSR Z-spectrum and used to correct B_0 inhomogeneity in the Z-spectra with $B_1 \in \{0.1, 0.5, 2\} \mu\text{T}$. The

Z-spectra with $B_1 \in \{3, 5\}$ μT were acquired with logarithmically spaced offsets (11 points from 300 to 3 ppm). Thus, B_0 correction was not required for these. Regions of interest (ROIs) were manually drawn on the high-resolution $T_1w + C$ images over the enhancing lesion, nonenhancing lesion (if any), and contralateral cortex and transformed into the Z-spectrum image space.

Magnetization transfer ratio asymmetry⁶² (MTR_{asym}) was calculated as follows:

$$\text{MTR}_{\text{asym}} = \frac{S(-\Delta\omega) - S(\Delta\omega)}{S_0}, \quad (1)$$

where $S(\Delta\omega)$ and $S(-\Delta\omega)$ are the measured voxel intensities after RF saturation at the frequency offsets $\Delta\omega$ and $-\Delta\omega$, respectively, and S_0 is that without saturation.

The parametric, longitudinal relaxation time T_1 map ($T_{1, \text{obs}}$) was calculated from the IR scans by fitting to the IR RARE data to a mono-exponential signal equation.⁵¹ The T_2 map ($T_{2, \text{obs}}$) was calculated from the CPMG scan by fitting the even echoes only (to avoid the effects of imperfect refocusing) to a mono-exponential decay function.

2.4 | Quantitative MT model fitting and isolation of CEST and rNOE contributions

MT, Z-spectra with $B_1 \in \{0.1, 3, 5\}$ μT were fitted to a two-pool quantitative MT⁶³ model using a super-Lorentzian line shape for the semisolid macromolecular pool for all voxels. The four free fitted parameters were the T_2 of the free pool ($T_{2, F}$), exchange rate of magnetization from the MT to the free pool (R_{MT}), equilibrium magnetization of the MT pool relative to the free pool ($M_{0, \text{MT}}$), and T_2 of the MT pool ($T_{2, \text{MT}}$). T_1 of the free pool was calculated from the observed T_1 , while T_1 of the macromolecular pool was assumed to be equal to 1 Hz.⁶³

Because Z-spectra are sensitive to direct water saturation, MT, CEST, and rNOE at different offset ranges, it was necessary to isolate each of them to reduce confounds. Based on the method introduced by Heo et al.,³⁶ the extrapolated semi-solid magnetization transfer reference (EMR) was calculated using the MT model parameters, which represents the MT effect. Adapting the technique described by Windschuh et al.,⁶⁴ the T_1 -corrected apparent exchange-dependent relaxation (AREX) metric for CEST and rNOE contributions was calculated as follows:

$$\text{MTR}_{\text{REX}} = \frac{1}{Z_{\text{lab}}} - \frac{1}{Z_{\text{EMR}}} \quad (2)$$

$$\text{AREX} = \frac{\text{MTR}_{\text{REX}}}{T_{1, \text{obs}}}, \quad (3)$$

where the measured Z-spectrum (with B_1 of 0.5 and 2 μT were each used) is denoted Z_{lab} , the extrapolated MT reference is Z_{EMR} , and the observed T_1 is $T_{1, \text{obs}}$.

Pre-processing and fitting were performed in MATLAB (R2018b; The MathWorks, Natick, MA) except for the image registration with FLIRT as noted above.

2.5 | Diffusion-weighted image processing

The fractional anisotropy, trace, trace-weighted, and diffusion tensor component images were calculated by the built-in macro in ParaVision.

2.6 | Statistical analysis

The mean values of various parameters: MTR (which is has CEST, MT, and T_1 weighting combined) at each frequency offset and saturation B_1 ; observed T_1 and T_2 relaxation ($T_{1, \text{obs}}$ and $T_{2, \text{obs}}$); quantitative MT model parameters ($T_{2, F}$, R_{MT} , $M_{0, \text{MT}}$, and $T_{2, \text{MT}}$), and AREX (CEST and rNOE contributions alone without MT and T_1 weighting) at ± 3.6 ppm and each saturation B_1 between enhancing lesion and contralateral cortex and between non-enhancing lesion and contralateral cortex ROIs (manually drawn on the $T_1w + C$ image and registered to the other images) were compared by pairwise Wilcoxon signed-rank tests with Holm–Bonferroni adjustment using the R Statistical Software⁶⁵ (v4.3.1). The frequency offset 3.6 ppm corresponds to the amide CEST peak position and -3.6 ppm to approximately the centre of the broad aliphatic rNOE peak.

2.7 | Lesion area estimation

The lesion on each single-slice MTR and AREX image (each at ± 3.6 ppm with a B_1 of $2 \mu\text{T}$) and $M_{0, \text{MT}}$ image was also delineated, and the lesion area calculated and compared with that estimated from the corresponding slice on the $T_1\text{W} + \text{C}$ image (in both native resolution and downsampled to match the saturation transfer image resolution to estimate the error from partial volume effects) to see which matched the latter the closest.

2.8 | Histopathology

Rats were sacrificed while under isoflurane anaesthesia. Then, brains were removed and post-fixed in 10% paraformaldehyde overnight. Next, paraffin-embedded brains were subsequently cut into $5\text{-}\mu\text{m}$ thick sections on a microtome (HM 360; Microm, Waldorf, Germany) and stained using haematoxylin and eosin (H&E). H&E staining was carried out to histologically confirm GBM morphology and evaluate TP.

3 | RESULTS

3.1 | MRI

Representative structural images; T_1 , T_2 , and MTR maps; and a diffusion trace image are shown in Figure 1 at each of the three imaging time points. The T_1 -weighted images ($T_1\text{W}$) show the needle track, but the lesion exhibits no contrast. The FLAIR images show hyperintense oedema and hypointense corpus callosum. On the T_1 -weighted post-injection images ($T_1\text{W} + \text{C}$), the hyperintense lesion is clearly visible at 3–5 and 7–9 days, which develops a hypointense core at 11–13 days. T_1 is approximately 1500 ms in normal appearing brain, whereas the lesion is characterized by increased T_1 (between 2000 and 2500 ms). Likewise, the transverse, observed relaxation time T_2 is approximately 50 ms in normal appearing brain, but 80 ms in the lesion. The ADC trace, ranging from 0.2 to $0.4 \mu\text{m}^2/\text{ms}$, does not appear to exhibit lesion contrast. Figure 2 shows the magnetization transfer ratio (MTR), quantitative MT model parameters maps, and CEST contribution to the signal (AREX) for a representative rat. The ROIs drawn on the $T_1\text{W} + \text{C}$ images are overlaid on the images. The lesion MTR is homogeneous and lower than that of normal appearing brain for both frequency offsets (amide and aliphatic), while the MTR asymmetry (MTR_{asym}) is elevated and more inhomogeneous. The fitted MT parameter transverse relaxation time T_2 of the free pool, $T_{2, \text{F}}$ is mildly longer (56 ± 6 ms in enhancing lesion vs 54 ± 5 ms in contralateral cortex at 3–5 days, 63 ± 7 vs 50 ± 7 ms at 7–9 days, and 65 ± 11 vs 53 ± 3 ms at 11–13 days). The lesion on the $M_{0, \text{MT}}$ and AREX maps with a B_1 of $2 \mu\text{T}$ are the both hypointense. The $2 \mu\text{T}$ MTR, $M_{0, \text{MT}}$, and $2 \mu\text{T}$ AREX maps (Figure 2) best match the shape of the hyperintensity on the $T_1\text{W} + \text{C}$ image (Figure 1).

Figure 3 presents the average CEST and MT Z-spectra across all rats at different time points for lesion ROIs and an ROI in the contralateral cortex. There is good separation in Z-spectra between the lesion (especially for high B_1 CEST) and contralateral cortex in the $2\text{-}\mu\text{T}$ CEST and 3- and $5\text{-}\mu\text{T}$ MT Z-spectra at all time points. Figure 3 also presents the Z-spectrum differences between lesion and cortex ROIs. Broad local maxima are evident in the MT Z-spectrum differences between lesions and cortex (at approximately 12 to 30 ppm) but less pronounced in the CEST Z-spectrum differences.

Figure 4 shows a summary of differences between enhancing lesion and contralateral cortex ROIs in MTR (with $B_1 = 2 \mu\text{T}$), observed T_1 ($T_{1, \text{obs}}$), relative macromolecular pool size ($M_{0, \text{MT}}$), and AREX (with $B_1 = 2 \mu\text{T}$). The differences between enhancing lesion ($n = 9$) and contralateral cortex for the $2\text{-}\mu\text{T}$ -saturation, amide-weighted MTR ($\text{MTR}_{3.6 \text{ ppm}, 2 \mu\text{T}}$: mean \pm SD of 57.4 ± 2.2 vs $61.2 \pm 0.8\%$, respectively, at 3–5 days after injection; 54.8 ± 2.2 vs $60.7 \pm 0.7\%$ at 7–9 days; and 56.1 ± 3.0 vs $60.8 \pm 1.0\%$ at 11–13 days), and relative macromolecular pool size ($M_{0, \text{MT}}$: 5.0 ± 0.9 vs $6.3 \pm 0.5\%$ at 3–5 days, 4.1 ± 1.1 vs $6.2 \pm 0.5\%$ at 7–9 days, and 4.6 ± 1.1 vs $6.5 \pm 0.4\%$ at 11–13 days) were strongly significant ($p < 0.001$) at all time points. The differences for the $2\text{-}\mu\text{T}$ -saturation, aliphatic-weighted MTR ($\text{MTR}_{-3.6 \text{ ppm}, 2 \mu\text{T}}$: 56.1 ± 3.8 vs $60.6 \pm 1.1\%$ at 3–5 days, 52.2 ± 4.1 vs $60.2 \pm 0.7\%$ at 7–9 days, and 55.0 ± 4.2 vs $59.8 \pm 1.2\%$ at 11–13 days), and amide and aliphatic AREX ($\text{AREX}_{3.6 \text{ ppm}, 2 \mu\text{T}}$: 0.23 ± 0.04 vs $0.28 \pm 0.04 \text{ s}^{-1}$ at 3–5 days, 0.21 ± 0.03 vs $0.29 \pm 0.02 \text{ s}^{-1}$ at 7–9 days, and 0.21 ± 0.04 vs $0.30 \pm 0.03 \text{ s}^{-1}$ at 11–13 days and $\text{AREX}_{-3.6 \text{ ppm}, 2 \mu\text{T}}$: 0.20 ± 0.06 vs $0.27 \pm 0.05 \text{ s}^{-1}$ at 3–5 days, 0.16 ± 0.06 vs $0.27 \pm 0.02 \text{ s}^{-1}$ at 7–9 days, and 0.19 ± 0.06 vs $0.27 \pm 0.04 \text{ s}^{-1}$ at 11–13 days) images were weakly significant ($p < 0.05$) at 3–5 days after implantation and strongly significant ($p < 0.001$) at 7–9 and 11–13 days. The difference for the observed T_1 images was not significant at 3–5 days after implantation ($T_{1, \text{obs}}$: 1750 ± 110 vs 1700 ± 80 ms), but grew in significance at 7–9 days (1910 ± 240 vs 1670 ± 120 ms, $p < 0.01$) and 11–13 days (1890 ± 150 vs 1590 ± 70 ms, $p < 0.001$). Comparisons between enhancing lesion and contralateral cortex for all metrics can be found in Supplementary Figure S2.

The differences between non-enhancing lesion ($n = 6$ at 3–5 days after implantation, $n = 5$ at 7–9 days, and $n = 8$ at 11–13 days) and contralateral cortex (Supplementary Figure S3) were significant at all time points for amide-weighted MTR ($\text{MTR}_{3.6 \text{ ppm}, 0.5 \mu\text{T}}$: 11.5 ± 0.5 vs $13.4 \pm 0.5\%$ at 3–5 days, $p < 0.01$; 11.5 ± 1.1 vs $13.5 \pm 0.6\%$ at 7–9 days, $p < 0.05$; and 11.7 ± 0.5 vs $13.4 \pm 0.5\%$ at 11–13 days, $p < 0.001$ and $\text{MTR}_{3.6 \text{ ppm}, 2 \mu\text{T}}$: 56.3 ± 2.6 vs $61.2 \pm 1.0\%$ at 3–5 days, $p < 0.01$; 53.0 ± 2.5 vs $60.7 \pm 0.8\%$ at 7–9 days, $p < 0.01$; and 53.1 ± 1.5 vs $60.9 \pm 0.9\%$

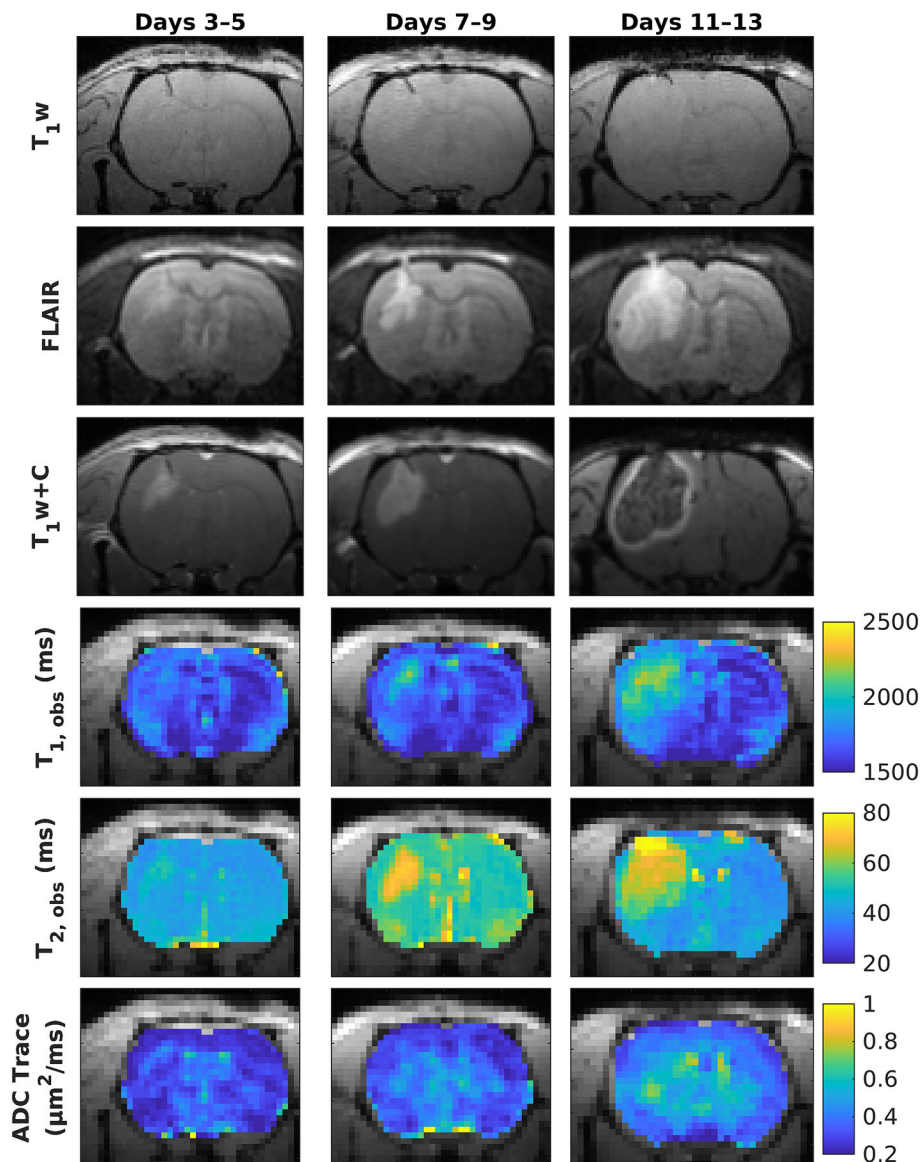


FIGURE 1 Representative cropped structural images, $T_{1, \text{obs}}$ and $T_{2, \text{obs}}$ maps, and ADC trace images. The time after implantation of U-87 MG cells is indicated. At 3–5 days, the acute reaction to the injection is evident; at 7–9 days, inflammation along the needle track and cancer cell mass resulting in hypointensity in the $T_{1w} + C$ image, and at 11–13 days, a vascular tumour resulting in hyperintensity in the $T_{1w} + C$ image. ADC, apparent diffusion coefficient.

at 11–13 days, $p < 0.001$) and $2 \mu\text{T}$ -saturation MTR asymmetry ($\text{MTR}_{\text{asym}, 2 \mu\text{T}}$: 2.7 ± 2.0 vs $0.2 \pm 0.3\%$ at 3–5 days, $p < 0.01$; 4.0 ± 1.5 vs $0.6 \pm 0.3\%$ at 7–9 days, $p < 0.01$; and 3.6 ± 1.0 vs $0.9 \pm 1.0\%$ at 11–13 days, $p < 0.001$). At 11–13 days, differences for aliphatic-weighted MTR ($\text{MTR}_{-3.6 \text{ ppm}, 0.5 \mu\text{T}}$: 14.7 ± 1.0 vs $19.3 \pm 0.6\%$ and $\text{MTR}_{-3.6 \text{ ppm}, 2 \mu\text{T}}$: 49.5 ± 1.7 vs $60.0 \pm 1.1\%$), $0.5 \mu\text{T}$ -saturation MTR asymmetry ($\text{MTR}_{\text{asym}, 0.5 \mu\text{T}}$: $-(3.0 \pm 0.9)$ vs $-(5.8 \pm 0.5)\%$), observed T_1 ($T_{1, \text{obs}}$: 2100 ± 220 vs 1590 ± 80 ms), relative macromolecular pool size ($M_{0, \text{MT}}$: 3.1 ± 0.7 vs $6.5 \pm 0.5\%$), and AREX ($\text{AREX}_{3.6 \text{ ppm}, 0.5 \mu\text{T}}$: 0.038 ± 0.005 vs $0.050 \pm 0.004 \text{ s}^{-1}$; $\text{AREX}_{-3.6 \text{ ppm}, 0.5 \mu\text{T}}$: 0.057 ± 0.010 vs $0.101 \pm 0.007 \text{ s}^{-1}$; $\text{AREX}_{3.6 \text{ ppm}, 2 \mu\text{T}}$: 0.186 ± 0.030 vs $0.306 \pm 0.034 \text{ s}^{-1}$; $\text{AREX}_{-3.6 \text{ ppm}, 2 \mu\text{T}}$: 0.116 ± 0.018 vs $0.272 \pm 0.043 \text{ s}^{-1}$) additionally become significant ($p < 0.001$).

The differences between enhancing and non-enhancing lesion (i.e., tumour regions with leaky and minimal vasculature, respectively; Supplementary Figure S4) were largely significant only at 11–13 days, when the tumour is vascularized, and mainly for 0.5 and $2 \mu\text{T}$ -saturation MTR asymmetry ($\text{MTR}_{\text{asym}, 0.5 \mu\text{T}}$: $-(5.1 \pm 0.9)$ vs $-(3.0 \pm 0.9)\%$, $p < 0.001$ and $\text{MTR}_{\text{asym}, 2 \mu\text{T}}$: 0.8 ± 1.0 vs $3.6 \pm 1.0\%$, $p < 0.001$); aliphatic-weighted MTR ($\text{MTR}_{-3.6 \text{ ppm}, 0.5 \mu\text{T}}$: 18 ± 2 vs $15 \pm 1\%$, $p < 0.01$ and $\text{MTR}_{-3.6 \text{ ppm}, 2 \mu\text{T}}$: 56 ± 3 vs $49 \pm 2\%$, $p < 0.01$), relative pool size and T_2 of the macromolecular pool ($M_{0, \text{MT}}$: 4.8 ± 4.0 vs $3.1 \pm 0.7\%$, $p < 0.01$ and $T_{2, \text{MT}}$: 9.1 ± 0.2 vs $8.7 \pm 0.2 \mu\text{s}$, $p < 0.01$), and aliphatic AREX ($\text{AREX}_{-3.6 \text{ ppm}, 0.5 \mu\text{T}}$: 0.08 ± 0.02 vs $0.06 \pm 0.01 \text{ s}^{-1}$, $p < 0.01$ and $\text{AREX}_{-3.6 \text{ ppm}, 2 \mu\text{T}}$: 0.21 ± 0.05 vs $0.12 \pm 0.02 \text{ s}^{-1}$, $p < 0.01$).

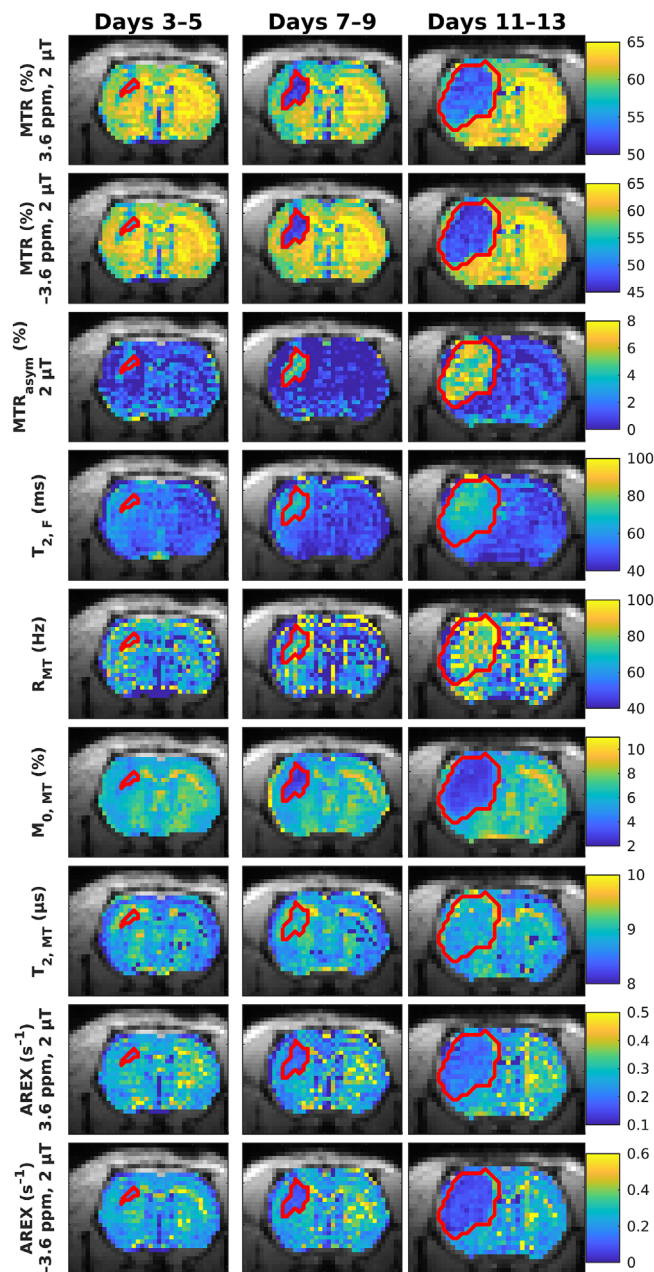


FIGURE 2 Representative MTR, MTR_{asym} , two-pool quantitative MT parameter, and AREX maps. The time after implantation of U-87 MG cells is indicated. See Supplementary Figure S1 for MTR, MTR_{asym} , and AREX maps with a saturation B_1 of $0.5 \mu T$. The ROIs drawn on the $T_1w + C$ images are overlaid. AREX, apparent exchange-dependent relaxation; MT, magnetization transfer; MTR, magnetization transfer ratio; ROIs, regions of interest.

Plots of the selected saturation transfer and relaxation parameters from Figure 4 vs time after cancer cell implantation in each ROI are shown in Figure 5. The contrasts have a trend (either increasing or decreasing depending on the contrast) in non-enhancing lesion (blue) but are largely constant over time in the contralateral cortex (grey). In both of these ROIs, the data are more tightly grouped than those in enhancing lesion (red). Also, the contrast values in the lesion ROIs only overlap with those of the contralateral cortex in a few cases, which indicates good discrimination.

The frequency offsets with the most significant differences between enhancing lesion and contralateral cortex ROIs for MTR and AREX both with a B_1 of $2 \mu T$ are listed in Table 1. Between enhancing lesion and contralateral cortex, differences in MTR were confined to a large range of positive offsets (at 5.6 to 4.6, 4.0 to 3.8, and 2.2 to 1.2 ppm; $p < 0.0001$) at 3–5 days after cell implantation but encompassed a large range of downfield and upfield offsets on subsequent days (at approximately 3.4 to 0.8 and -1.2 to -4 ppm; $p < 0.0001$). Differences in AREX at 3–5 days after cell implantation only reached $p < 0.001$ significance (at 1.6 ppm) but reached $p < 0.0001$ significance on subsequent days (at approximately 3.4 to 1.2 and -3.4 to -3.6 ppm). No single-frequency offset was identified as the most significant by the test used, which

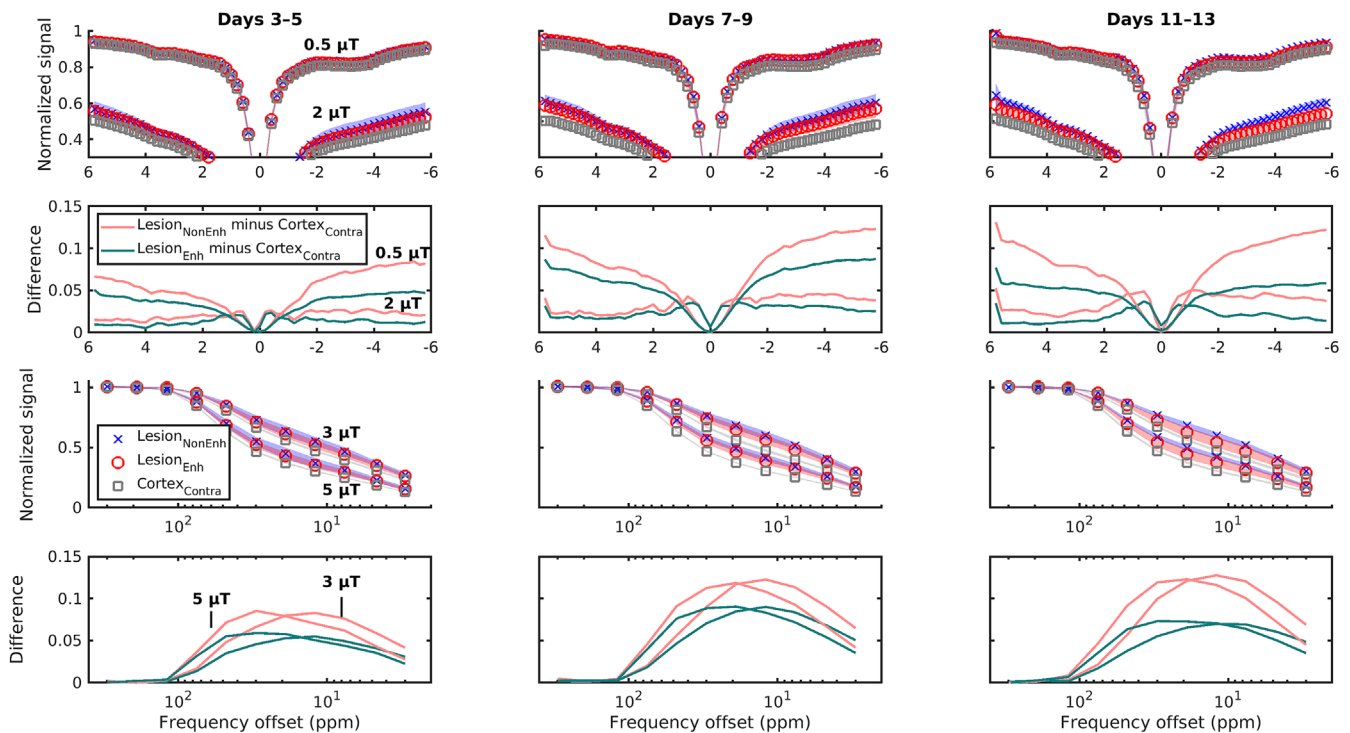


FIGURE 3 Mean Z-spectra in non-enhancing and enhancing lesion and contralateral cortex ROIs and Z-spectrum differences between lesion and cortex ROIs. The time after implantation of U-87 MG cells and saturation B_1 are indicated. Shaded areas in the Z-spectra indicate SD across all rats. The SD is omitted from the difference plots for clarity. ROIs, regions of interest; SD, standard deviation.

agrees with the lack of any prominent local maximum in the CEST (low- B_1) Z-spectrum difference plots in Figure 3. Statistical significance levels at all offsets are listed in Supplementary Tables S4 and S5.

The use of six diffusion directions allowed us to analyse only the trace and trace-weighted images because the other parameters calculated from tensor fitting (i.e., the fractional anisotropy; apparent diffusion coefficients λ_1 , λ_2 , and λ_3 along the principal, secondary, and tertiary diffusion directions, respectively, which make up the tensor diagonal elements; and tensor cross terms) had an insufficient contrast-to-noise ratio. Only the trace-weighted image (but not the trace image) showed a strong difference between enhancing lesion and contralateral cortex and only at 11–13 days (Supplementary Figure S5), which was not exhibited between non-enhancing lesion and contralateral cortex (Supplementary Figure S6) nor between enhancing and non-enhancing lesion (Supplementary Figure S7).

A plot of single-slice lesion area (on the $T_1W + C$; MTR and ARES [± 3.6 ppm, 2 μT]; and M_0 , M_T images) versus time after cancer cell implantation is shown in Figure 6. One lesion was identified as an outlier and omitted from calculations because its area was 8%–18% of the mean area of the other lesions as measured on the native (high) resolution $T_1W + C$ images. The lesion area over time, also measured from the native resolution $T_1W + C$ images, appeared to increase exponentially (with an adjusted R^2 of 0.99 when fitted to an exponential model compared to 0.97 for a linear model). The area estimated from the downsampled (lower-resolution) $T_1W + C$ images was up to 7% smaller than that from the native resolution $T_1W + C$ images, so the downsampled images were used for comparison with the other images types, which were acquired at lower resolution. The areas calculated from the other images types were similar to each other and smaller than those from the $T_1W + C$. Areas on MTR_{3.6 ppm, 2 μT} images were 25%, 13%, and 14% lower than those on $T_1W + C$ at 3–5, 7–9, and 11–13 days after cell implantation, respectively; areas on MTR_{-3.6 ppm, 2 μT} images were 32%, 17%, and 19% lower; areas on M_0 , M_T images were 21%, 6%, and 14% lower; areas on ARES_{3.6 ppm, 2 μT} images were 20%, 14%, and 16% lower; and areas on ARES_{-3.6 ppm, 2 μT} images were 34%, 14%, and 21% lower.

3.2 | Histopathology

Haematoxylin and eosin staining was performed on each brain (on days 13 to 14 after cell implantation when animals were sacrificed) and a representative tumour slice is shown in Figure 7. H&E-based tissue morphology presented substantial development of the glioma within the right hemisphere (Figure 7A). The magnified image of the lesion displays homogeneity in cell structure (Figure 7B): the area of tumour is well defined, and no infiltrating cells in healthy brain tissue are visible.

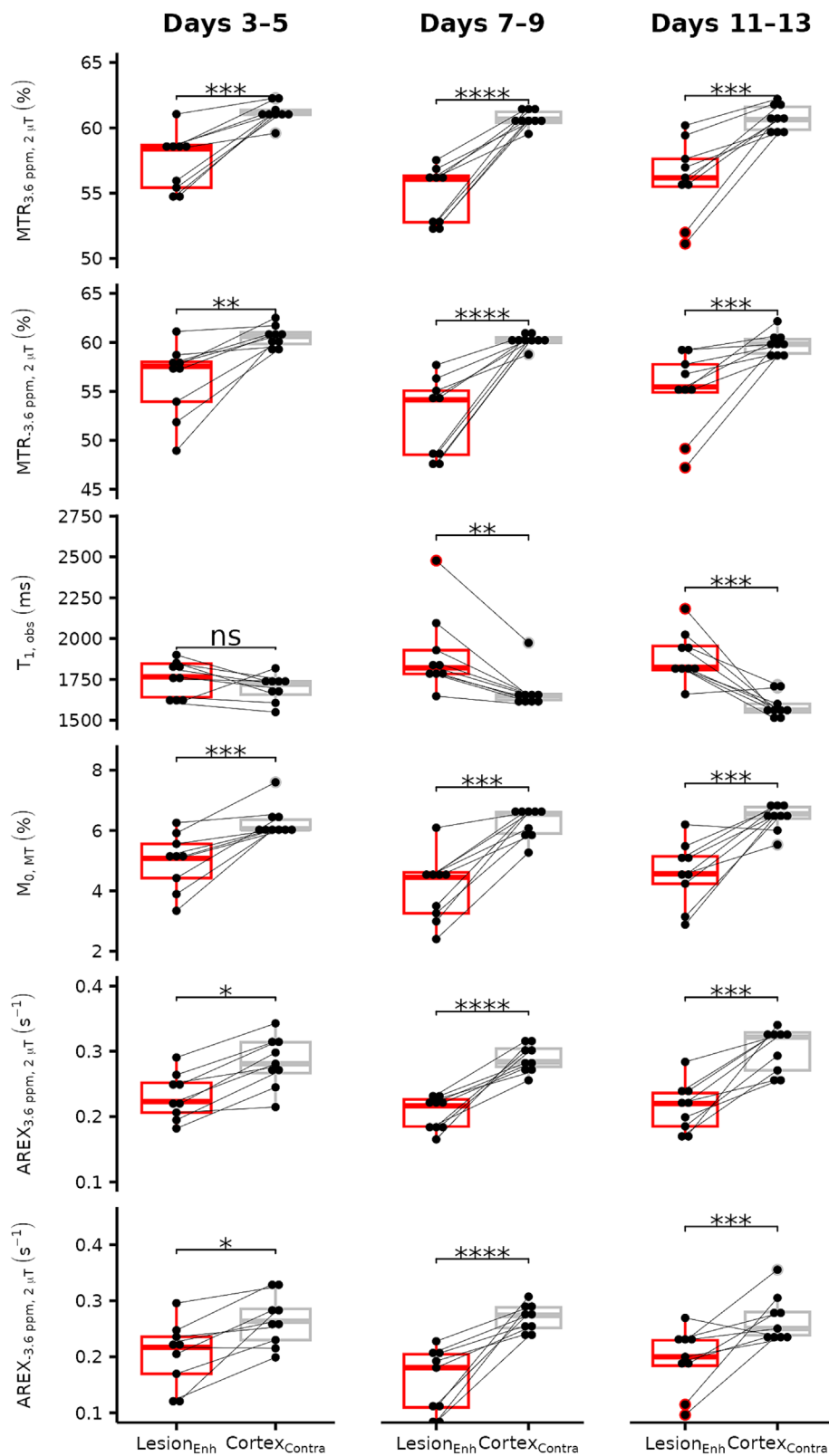


FIGURE 4 Comparison of selected saturation transfer and relaxation parameters in enhancing lesion and contralateral cortex ROIs. Box plots show the MTR at the amide offset of 3.6 ppm and the aliphatic of -3.6 ppm with a B_1 of $2 \mu\text{T}$, observed T_1 ($T_{1, \text{obs}}$), MT pool size (M_0, MT) relative to that of water from the two-pool quantitative MT model, and AREX metric, which represents the CEST effect without the influence of T_1 nor MT. The time after implantation of U-87 MG cells is indicated. Significant differences, by pairwise Wilcoxon signed rank tests with Holm–Bonferroni adjustment, are also indicated. * $p < 0.05$, ** $p < 0.01$, *** $p < 0.001$, **** $p < 0.0001$. See Supplementary Figures S2–S7 for boxplots for all parameters and pairwise ROI comparisons. CEST, chemical exchange saturation transfer; MT, magnetization transfer; MTR, magnetization transfer ratio; ROIs, regions of interest.

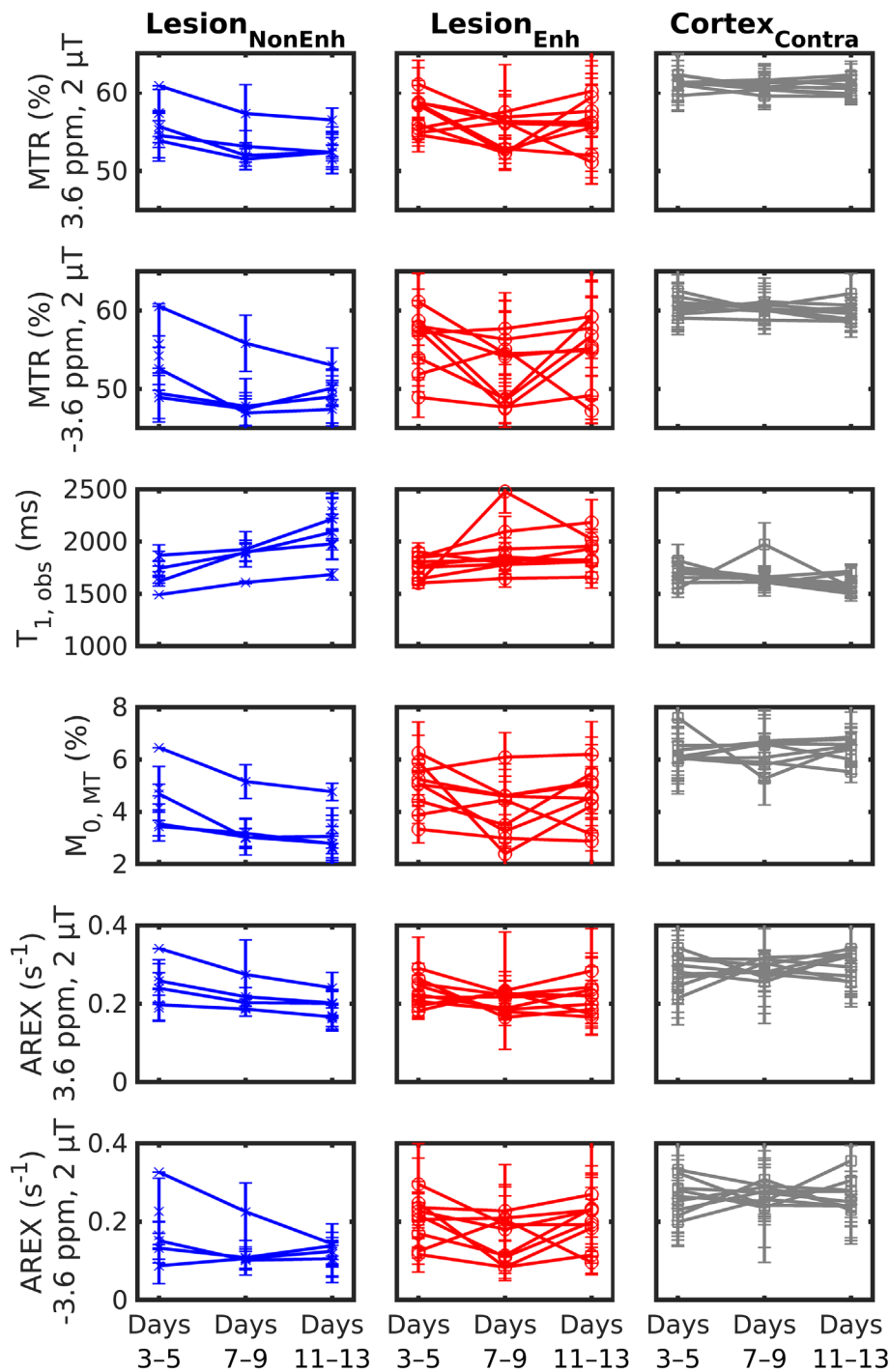


FIGURE 5 Plots of the selected saturation transfer and relaxation parameters from Figure 4 vs time after cancer cell implantation in non-enhancing lesion, enhancing lesion, and contralateral cortex ROIs. Non-enhancing lesion was not present at all time points. Hence, some measurements (blue crosses) are not connected by lines. Error bars represent SD across ROI voxels per animal. ROIs, regions of interest; SD, standard deviation.

4 | DISCUSSION

An orthotopic model of glioma was utilized to characterize malignant glioma with conventional and novel CEST and MT MRI at three time points. At 3–5 days after implantation, the acute reaction to the implantation was evident; at 7–9 days, inflammation along the needle track and cancer cell mass was present resulting in hypointensity in the $T_{1w} + C$ image; and, at 11–13 days, a vascular tumour resulting in hyperintensity in the $T_{1w} + C$ image was observed. The best observed contrast between enhancing lesion and contralateral cortex was found with the MTR image with

TABLE 1 Frequency offsets with the most significant differences between enhancing lesion and contralateral cortex ROIs for MTR and AREX both with a B_1 of $2 \mu\text{T}$ at all time points. For each case (MTR or AREX at each time point for each pair of ROIs compared), only the offsets with the most significant differences, by pairwise Wilcoxon signed rank tests with Holm–Bonferroni adjustment, are listed.

Metric	Frequency offsets with the most significant differences		
	Days 3–5	Days 7–9	Days 11–13
MTR ($2 \mu\text{T}$)	5.6 to 4.6 ppm, 4.0 to 3.8 ppm, 2.2 to 1.2 ppm****	5.6 to 0.8 ppm, –0.8 to –5.8 ppm****	3.4 to 0.8 ppm, –1.2 to –1.6 ppm, –2.0 to –2.6 ppm, –3.2 to –3.4 ppm, –4.0 ppm****
AREX ($2 \mu\text{T}$)	1.6 ppm***	5.8 ppm, 5.0 ppm, 4.0 to 1.2 ppm, –3.4 to –3.6 ppm****	3.8 ppm, 3.4 to 1.2 ppm, –2.4 to –3.6 ppm, –4.0 ppm****

Abbreviations: AREX, apparent exchange-dependent relaxation; MTR, magnetization transfer ratio; ROIs, regions of interest.

*** $p < 0.001$, and **** $p < 0.0001$.

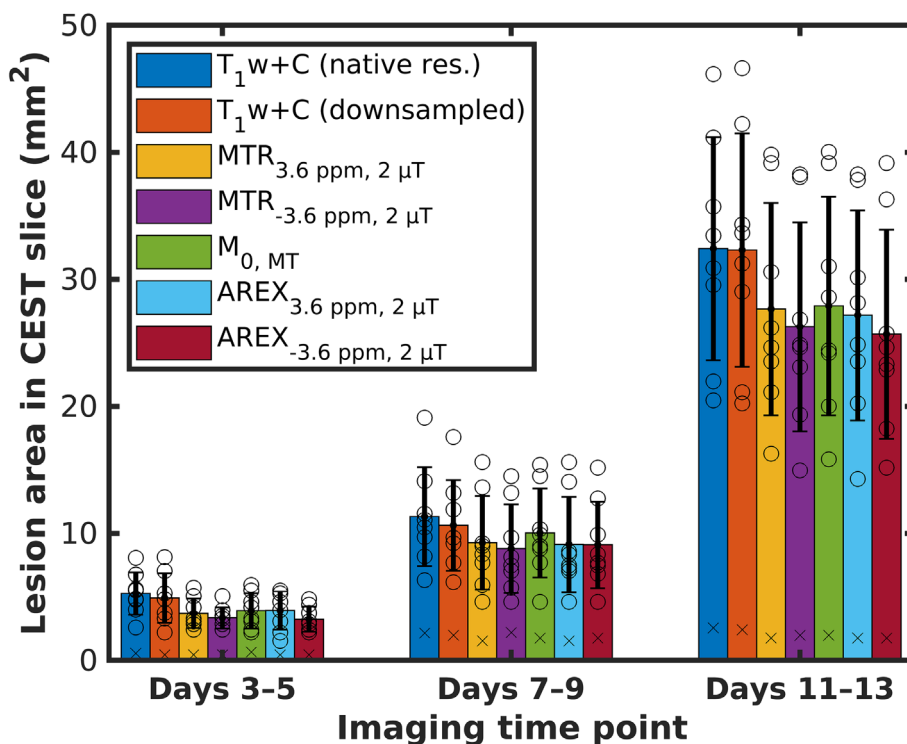


FIGURE 6 A plot of single-slice lesion area versus time after cancer cell implantation. ROIs were drawn separately on each of the following image types: $T_1W + C$ (native resolution and downsampled to match the resolution of the saturation transfer images), MTR and AREX (± 3.6 ppm, $2 \mu\text{T}$), and $M_{0, \text{MT}}$. Bars show the mean area; error bars, SD; circles, measurements from individual lesions; and crosses, measurements from the lesion identified as an outlier, which were omitted from the mean and SD. AREX, apparent exchange-dependent relaxation; MTR, magnetization transfer ratio; ROIs, regions of interest; SD, standard deviation.

$2 \mu\text{T}$ saturation at 3.6 ppm frequency offset (corresponding to the amide chemical group) and in the MT macromolecular pool ($M_{0, \text{MT}}$) parametric map. Both were strongly significant ($p < 0.001$) at all time points.

Our results agreed qualitatively with those of Zhou et al.,³⁹ who have imaged Fischer 344 rats ($n = 8$) with 9 L glioblastoma tumours (while nude rats with U-87 MG tumours were used in the present work) at 4.7 T at 9–12 days after implantation using CEST Z-spectra. We measured a 7–9-day post-implantation MTR asymmetry with $B_1 = 0.5 \mu\text{T}$ of $-(4 \pm 1)\%$ (mean \pm SD) and with $B_1 = 2 \mu\text{T}$ of $3 \pm 2\%$, which was higher than that of contralateral brain. Zhou et al. report MTR asymmetry with low B_1 ($0.6 \mu\text{T}$) of -1.5% and with high B_1 ($2.1 \mu\text{T}$) of $\approx 4\%$, which is also higher

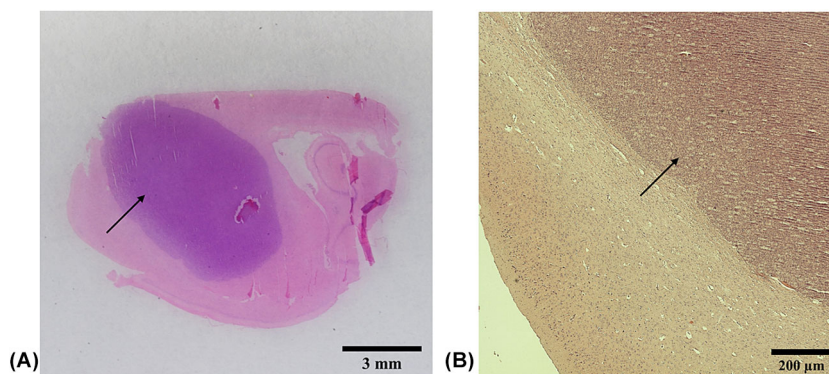


FIGURE 7 Histopathological sections stained with haematoxylin and eosin (H&E) of the same rat as in Figure 1. That rat was scanned on MRI at 3, 7, and 11 days after cancer cell implantation and sacrificed at 14 days. (A) Macroscopic and (B) magnified ($10\times$) images of a sagittal slice with a tumour (arrow) in the right hemisphere. MRI, magnetic resonance imaging.

than that of contralateral brain. Quantitative differences between the present work and the results of Zhou et al. likely stem from the different magnetic field used. They can also be related to different cell lines and, hence, different tumour metabolism.

Relaxation and MT measurements in the present work were also comparable with those in literature. Xu et al.³⁷ have characterized Fischer 344 rats ($n = 8$) with 9 L glioblastoma tumours at 9.4 T at 14–18 days after implantation. Likewise, Heo et al.³⁶ report data for Fischer 344 rats ($n = 6$) with glioblastoma tumours at 4.7 T at 45 days after implantation. At 11–13 days, we observed a T_1 of 1890 ± 150 ms and T_2 of 50 ± 10 ms. Xu et al. report values of 2100 ± 300 and 36 ± 3 ms, respectively, and Heo et al. estimate the tumour rim T_1 to be 1880 ± 50 ms. The quantitative MT model parameters in this study were $T_{2, F}$: 63 ± 7 ms, R_{MT} : 66 ± 10 Hz, $M_{0, MT}$: $4.6 \pm 1.1\%$, and $T_{2, MT}$: 9.1 ± 0.2 μ s, whereas Xu et al. estimate an R_{MT} (denoted k_{mf}) of 20 ± 3 Hz, and $M_{0, MT}$ (denoted pool size ratio) of $5.7 \pm 1.0\%$, while Heo et al. report a $T_{2, F}$ (denoted T_{2w}) of 65 ± 0.8 ms, R_{MT} (denoted R) of 22 ± 1 Hz, $M_{0, MT}$ (denoted M_{0m}) of $3.1 \pm 0.2\%$, and $T_{2, MT}$ (denoted T_{2m}) of 18 ± 1 μ s. We measured an ADC trace of 0.2 ± 0.1 $\mu\text{m}^2/\text{ms}$ at 3–5 days, 0.2 ± 0.2 $\mu\text{m}^2/\text{ms}$ at 7–9 days, and 0.4 ± 0.2 $\mu\text{m}^2/\text{ms}$ at 11–13 days. Xu et al. reported 0.8 ± 0.1 $\mu\text{m}^2/\text{ms}$ at 14–18 days, which continues the trend that we measured.

Similar contrast has also been found in human CEST images. Our MTR asymmetry at 11–13 days with $B_1 = 0.5$ μT at ± 3.6 ppm of $-(5 \pm 1)\%$ was comparable with that measured by Heo et al.⁶⁶ at 7 T with 0.54 μT pulsed saturation (whereas we used continuous-wave) in grade 2 and 3 gliomas of $\approx -2\%$. Our estimated AREX (also at 11–13 days) with $B_1 = 0.5$ μT at 3.6 and -3.6 ppm of 0.040 ± 0.006 and 0.08 ± 0.02 s^{-1} , respectively, matched those measured by Dreher et al.⁶⁷ at 7 T with 0.6 μT pulsed saturation in grade 4 gliomas of ≈ 0.045 and ≈ 0.1 s^{-1} , respectively.

Our finding of significant contrast between enhancing lesion and contralateral cortex in the MTR images with 2 μT saturation at 3.6 and -3.6 ppm frequency offset (corresponding to the amide and aliphatic chemical groups, respectively; first and second rows in Figure 4) was in line with the recent consensus paper.⁶⁸ This lends support to the application of APT-weighted imaging to show tumour contrast at 3 T with 2 s saturation duration and potentially of single-offset MTR imaging at 3.6 or -3.6 ppm at 7 T with steady state saturation. The clinically recommended APT asymmetry contrast only acquires images saturated at ± 3.5 ppm with a few nearby offsets acquired for interpolation after B_0 inhomogeneity correction, which can shift the Z-spectrum left or right. That is the reason why 3.6 ppm, our nearest measurement, was chosen for assessment. The offsets near ± 3.5 ppm appear to capture the most significant differences for vascularized tumour at 11–13 days after cancer cell implantation (Table 1). Also, the relative MT pool size estimated from the quantitative MT model appears to have as much contrast as APT.

APT-weighted contrast includes APT CEST contrast, around 3.6 ppm; rNOE, around -3.6 ppm, and MT, which is largely symmetric between downfield and upfield frequency offsets. The data presented in this work isolated each contrast (APT and rNOE were isolated using the AREX metric and MT using quantitative modelling). Each contrast is mechanistically unique and may be clinically relevant. APT CEST reflects amide protons mainly from mobile proteins. rNOE reflects mobile macromolecules with aliphatic chemical groups. MT is sensitive to immobile semisolid macromolecules such as lipids found in cell membranes. They may reflect different aspects of tissue metabolism and microstructure that may be useful in differentiation between different tumour types.

An animal model at 7 T can provide clinically relevant guidance for 3 T scans because an animal study should have less inter-subject variability compared to a clinical study due to the use of a single animal strain and cancer cell line and common subject history. This aids the characterization of the most significant differences in lesion contrast compared with that of normal brain. Compared to 3 T, the line widths at 7 T are narrower, which leads to less contamination of the amide (≈ 3.6 ppm) peak by neighbouring ones, such as from that of guanidinium (2 ppm). Thus, this study has the most clinical relevance at 7 T, but the identified contrasts of interest may still be relevant at lower fields.

The MTR contrasts are scanner-dependent because they reflect the sequence-dependent saturation pulse parameters (specifically, the frequency offsets at ± 3.6 ppm and B_1 of 2 μT can be replicated clinically, but the 4.9-s duration used in the present work to achieve

steady-state saturation would be prohibitive due to radiofrequency energy specific absorption rate and acquisition time limitations) and field-strength-dependent tissue T_1 . Steady-state (maximal) saturation is achieved when the duration is approximately five times the T_1 value of the saturated tissue, which was the goal in this work. A shorter duration results in less contrast. However, sufficient tumour contrast on APTw images at 3 T has been shown to require a saturation duration of 1–2 s.⁶⁸ The trade-off between acquisition time and tumour contrast will have to be optimized for a given field strength and tissue characteristics. The optimal macromolecular (MT) relative pool size ratio image is scanner-independent because it is estimated from a quantitative model and can be translated successfully to different field strengths.^{41,69}

Our estimate of exponential lesion area growth was in line with the exponential volume growth measured by Walsh et al.⁷⁰ who have performed multiparametric measurements of U-87 tumours in rats at 11.7 T starting at 10–28 days after cancer cell implantation and every 4–7 days thereafter. We also found that the mean lesion area calculated from the MTR and AREX (± 3.6 ppm, 2 μ T) and $M_{0, MT}$ images generally matched closely with each other, but were all 6% to 34% smaller than that measured in the corresponding slice on the $T_1w + C$. None were consistently closer to the area estimated from the $T_1w + C$ at all time points. This could be due to extravasation of contrast agent from the lesion, which does not occur using endogenous CEST and MT contrast.

The U-87 line is one of the most widely used human GBM cell lines in the literature (with over 2000 publications⁷¹) and carries a number of human GBM characteristics such as a population of glioblastoma stem cells (CD133⁺) cells⁷²; some of the molecular characteristics of human GBMs such as hTERT, ATRX, and PTEN mutations; a lack of p53 or IDH1 mutations; and methylated MGMT status.^{73,74} Moreover, it has been proven that it readily responds to standard therapy protocols with temozolomide and radiation.^{75,76} Therefore, even though it lacks some of the clinical features of human GBMs such as diffuse infiltration⁷⁷ or the presence of higher levels of 'leaky' vessels, that potentially increases the access of systemic drugs to the tumour microenvironment,⁷⁸ it has been extensively used in orthotopic xenograft models in order to study novel therapeutic modalities along with its translational potential.^{79–82} Our findings provided additional information regarding the xenograft microenvironment that will certainly strengthen our understanding of xenograft response to various therapeutic systems testable in the described model. Therefore, even though our model did not perfectly represent a clinical GBM, our findings might shed a new light on the mechanisms related to therapeutic systems' response within its limits and in this respect should allow one to project the probable response patterns to a given therapeutic system in a clinical situation.

Finally, it was notable that gadolinium contrast agent was not required to identify the tumour, which has been shown clinically at 3 T with MTR asymmetry (with 2 μ T saturation at ± 3.5 ppm).⁴³ Even the entire Z-spectrum may not be required to screen for the presence of tumour at 7 T as the lesion had high contrast in a single MTR image (with 2 μ T at 3.6 ppm) in the present work. The use of MTR instead of MTR asymmetry would require fewer images (i.e., no need to acquire around -3.6 ppm) and reduce acquisition time.

This work has identified that differences between enhancing lesion and contralateral cortex are strongest in MTR with $B_1 = 2$ μ T at 3.6 ppm (corresponding to the amide chemical group) and relative macromolecular pool size ($M_{0, MT}$) images over entire period of 3–13 days after cancer cell implantation.

ACKNOWLEDGMENTS

The authors thank the following sponsors: the Medical University of Lublin (grant numbers: PBmd230 and DS316), the Terry Fox Research Institute (grant number: 1115-03), and the Canadian Cancer Society (grant number: 705083). The authors also thank the staff of the Pathomorphology Laboratory in the Department of Neurosurgery and Paediatric Neurosurgery for performing H&E staining and Margaret Koletar for helpful discussion.

CONFLICT OF INTEREST STATEMENT

The authors declare no conflicts of interest.

DATA AVAILABILITY STATEMENT

The data that support the findings of this study are available from the corresponding author upon reasonable request.

ORCID

Wilfred W. Lam  <https://orcid.org/0000-0002-9883-6142>

Anna Orzyłowska  <https://orcid.org/0000-0001-7457-0725>

REFERENCES

- Goel NJ, Bird CE, Hicks WH, Abdullah KG. Economic implications of the modern treatment paradigm of glioblastoma: an analysis of global cost estimates and their utility for cost assessment. *J Med Econ.* 2021;24(1):1018–1024. doi:10.1080/13696998.2021.1964775
- Mohammed S, Dinesan M, Ajayakumar T. Survival and quality of life analysis in glioblastoma multiforme with adjuvant chemoradiotherapy: a retrospective study. *Rep Pract Oncol Radiother.* 2022;27(6):1026–1036. doi:10.5603/RPOR.a2022.0113

3. Grech N, Dallì T, Mizzi S, Meilak L, Calleja N, Zrinzo A. Rising incidence of glioblastoma multiforme in a well-defined population. *Cureus*. 2020;12(5):e8195. doi:10.7759/cureus.8195
4. Yang D. Standardized MRI assessment of high-grade glioma response: a review of the essential elements and pitfalls of the RANO criteria. *Neuro-Oncol Pract*. 2016;3(1):59-67. doi:10.1093/nop/npv023
5. Zhou Q, Xue C, Ke X, Zhou J. Treatment response and prognosis evaluation in high-grade glioma: An imaging review based on MRI. *J Magn Reson Imaging*. 2022;56(2):325-340. doi:10.1002/jmri.28103
6. Bonm AV, Ritterbusch R, Throckmorton P, Graber JJ. Clinical imaging for diagnostic challenges in the management of gliomas: a review. *J Neuroimaging*. 2020;30(2):139-145. doi:10.1111/jon.12687
7. Booth TC, Wiegers EC, Warnert EAH, et al. High-grade glioma treatment response monitoring biomarkers: a position statement on the evidence supporting the use of advanced MRI techniques in the clinic, and the latest bench-to-bedside developments. Part 2: spectroscopy, chemical exchange saturation, multiparametric imaging, and radiomics. *Front Oncologia*. 2022;11:811425. doi:10.3389/fonc.2021.811425
8. Henriksen OM, del Mar Á-TM, Figueiredo P, et al. High-grade glioma treatment response monitoring biomarkers: a position Statement on the evidence supporting the use of advanced MRI techniques in the clinic, and the latest bench-to-bedside developments. Part 1: perfusion and diffusion techniques. *Front Oncologia*. 2022;12:810263. doi:10.3389/fonc.2022.810263
9. Leao DJ, Craig PG, Godoy LF, Leite CC, Policeni B. Response assessment in neuro-oncology criteria for gliomas: practical approach using conventional and advanced techniques. *Am J Neuroradiol*. 2020;41(1):10-20. doi:10.3174/ajnr.A6358
10. Stupp R, Mason WP, van den Bent MJ, et al. Radiotherapy plus concomitant and adjuvant temozolomide for glioblastoma. *N Engl J Med*. 2005;352(10):987-996. doi:10.1056/NEJMoa043330
11. Ceccon G, Lohmann P, Werner JM, et al. Early treatment response assessment using ¹⁸F-FET PET compared with contrast-enhanced MRI in glioma patients after adjuvant Temozolomide chemotherapy. *J Nucl Med*. 2021;62(7):918-925. doi:10.2967/jnumed.120.254243
12. Forsyth PA, Kelly PJ, Cascino TL, et al. Radiation necrosis or glioma recurrence: is computer-assisted stereotactic biopsy useful? *J Neurosurg*. 1995;82(3):436-444. doi:10.3171/jns.1995.82.3.0436
13. Gerstner ER, McNamara MB, Norden AD, LaFrankie D, Wen PY. Effect of adding temozolomide to radiation therapy on the incidence of pseudoprogression. *J Neurooncol*. 2009;94(1):97-101. doi:10.1007/s11060-009-9809-4
14. van Dijken BRJ, van Laar PJ, Holtman GA, van der Hoorn A. Diagnostic accuracy of magnetic resonance imaging techniques for treatment response evaluation in patients with high-grade glioma, a systematic review and meta-analysis. *Eur Radiol*. 2017;27(10):4129-4144. doi:10.1007/s00330-017-4789-9
15. Taylor C, Ekert JO, Sefcikova V, Fersht N, Samandouras G. Discriminators of pseudoprogression and true progression in high-grade gliomas: a systematic review and meta-analysis. *Sci Rep*. 2022;12(1):13258. doi:10.1038/s41598-022-16726-x
16. Corroyer-Dulmont A, Pérès EA, Petit E, et al. Detection of glioblastoma response to temozolomide combined with bevacizumab based on μ MRI and μ PET imaging reveals [¹⁸F]-fluoro-l-thymidine as an early and robust predictive marker for treatment efficacy. *Neuro-Oncol*. 2013;15(1):41-56. doi:10.1093/neuonc/nos260
17. Chen D, Zhou Y, Yang D, et al. Positron emission tomography/magnetic resonance imaging of glioblastoma using a functionalized gadofullerene nanoparticle. *ACS Appl Mater Interfaces*. 2019;11(24):21343-21352. doi:10.1021/acsami.9b03542
18. Jalali S, Chung C, Foltz W, et al. MRI biomarkers identify the differential response of glioblastoma multiforme to anti-angiogenic therapy. *Neuro-Oncol*. 2014;16(6):868-879. doi:10.1093/neuonc/nou040
19. Pechman KR, Donohoe DL, Bedekar DP, Kurpad SN, Hoffmann RG, Schmainda KM. Characterization of bevacizumab dose response relationship in U87 brain tumors using magnetic resonance imaging measures of enhancing tumor volume and relative cerebral blood volume. *J Neurooncol*. 2011;105(2):233-239. doi:10.1007/s11060-011-0591-8
20. Claes A, Gambarota G, Hamans B, et al. Magnetic resonance imaging-based detection of glial brain tumors in mice after antiangiogenic treatment. *Int J Cancer*. 2008;122(9):1981-1986. doi:10.1002/ijc.23306
21. Doblas S, He T, Saunders D, et al. Glioma morphology and tumor-induced vascular alterations revealed in seven rodent glioma models by in vivo magnetic resonance imaging and angiography. *J Magn Reson Imaging*. 2010;32(2):267-275. doi:10.1002/jmri.22263
22. Zavjalov EL, Razumov IA, Gerlinskaya LA, Romashchenko AV. In vivo MRI visualization of U87 glioblastoma development dynamics in the model of orthotopic xenotransplantation to the SCID mouse. *Russ J Genet Appl Res*. 2016;6(4):448-453. doi:10.1134/S2079059716040225
23. Li J, Huang S, Shao K, et al. A choline derivate-modified nanoprobe for glioma diagnosis using MRI. *Sci Rep*. 2013;3(1):1623. doi:10.1038/srep01623
24. Linnik IV, Scott MLJ, Holliday KF, et al. Noninvasive tumor hypoxia measurement using magnetic resonance imaging in murine U87 glioma xenografts and in patients with glioblastoma. *Magn Reson Med*. 2014;71(5):1854-1862. doi:10.1002/mrm.24826
25. Tong AN, Lv XY, Yan P, Wang YM. Magnetic resonance T2*-weighted study of U87 MG glioma tumors and its relationship between tumor hypoxia and VEGF expression. *CNS Neurosci Ther*. 2013;19(3):201-203. doi:10.1111/cns.12055
26. Sun Y, Schmidt NO, Schmidt K, et al. Perfusion MRI of U87 brain tumors in a mouse model. *Magn Reson Med*. 2004;51(5):893-899. doi:10.1002/mrm.20029
27. Flament J, Geffroy F, Medina C, et al. In vivo CEST MR imaging of U87 mice brain tumor angiogenesis using targeted LipoCEST contrast agent at 7 T. *Magn Reson Med*. 2013;69(1):179-187. doi:10.1002/mrm.24217
28. Sun Y, Mulkern RV, Schmidt K, et al. Quantification of water diffusion and relaxation times of human U87 tumors in a mouse model. *NMR Biomed*. 2004;17(6):399-404. doi:10.1002/nbm.894
29. Mehrabian H, Chan RW, Sahgal A, et al. Chemical exchange saturation transfer MRI for differentiating radiation necrosis from tumor progression in brain metastasis—application in a clinical setting. *J Magn Reson Imaging*. 2023;57(6):1713-1725. doi:10.1002/jmri.28440
30. von Knebel DN, Kroh F, Breitling J, et al. CEST imaging of the APT and ssMT predict the overall survival of patients with glioma at the first follow-up after completion of radiotherapy at 3T. *Radiother Oncol*. 2023;184:109694. doi:10.1016/j.radonc.2023.109694
31. Zhou J, Tryggstad E, Wen Z, et al. Differentiation between glioma and radiation necrosis using molecular magnetic resonance imaging of endogenous proteins and peptides. *Nat Med*. 2011;17(1):130-134. doi:10.1038/nm.2268
32. Henkelman RM, Stanisz GJ, Graham SJ. Magnetization transfer in MRI: a review. *NMR Biomed*. 2001;14(2):57-64. doi:10.1002/nbm.683
33. van Zijl PCM, Lam WW, Xu J, Knutsson L, Stanisz GJ. Magnetization transfer contrast and chemical exchange saturation transfer MRI. Features and analysis of the field-dependent saturation spectrum. *Neuroimage*. 2018;168:222-241. doi:10.1016/j.neuroimage.2017.04.045

34. Zhou Y, Bie C, van Zijl PCM, Yadav NN. The relayed nuclear Overhauser effect in magnetization transfer and chemical exchange saturation transfer MRI. *NMR Biomed*. 2023;36(6):e4778. doi:10.1002/nbm.4778
35. Chen X, Wei X, Liu L, et al. Comparison of the reproducibility of 2D and 3D amide proton transfer weighted imaging in intracranial rat gliomas at 3 T. *Chin J Acad Radiol*. 2020;3(1):59-64. doi:10.1007/s42058-020-00028-0
36. Heo HY, Zhang Y, Lee DH, Hong X, Zhou J. Quantitative assessment of amide proton transfer (APT) and nuclear Overhauser enhancement (NOE) imaging with extrapolated semi-solid magnetization transfer reference (EMR) signals: application to a rat glioma model at 4.7 tesla. *Magn Reson Med*. 2016;75(1):137-149. doi:10.1002/mrm.25581
37. Xu J, Li K, Zu Z, Li X, Gochberg DF, Gore JC. Quantitative magnetization transfer imaging of rodent glioma using selective inversion recovery. *NMR Biomed*. 2014;27(3):253-260. doi:10.1002/nbm.3058
38. Zhou IY, Wang E, Cheung JS, Zhang X, Fulci G, Sun PZ. Quantitative chemical exchange saturation transfer (CEST) MRI of glioma using image downsampling expedited adaptive least-squares (IDEAL) fitting. *Sci Rep*. 2017;7(1):84. doi:10.1038/s41598-017-00167-y
39. Zhou J, Hong X, Zhao X, Gao JH, Yuan J. APT-weighted and NOE-weighted image contrasts in glioma with different RF saturation powers based on magnetization transfer ratio asymmetry analyses. *Magn Reson Med*. 2013;70(2):320-327. doi:10.1002/mrm.24784
40. Meissner JE, Korzowski A, Regnery S, et al. Early response assessment of glioma patients to definitive chemoradiotherapy using chemical exchange saturation transfer imaging at 7 T. *J Magn Reson Imaging*. 2019;50(4):1268-1277. doi:10.1002/jmri.26702
41. Mehrabian H, Myrehaug S, Soliman H, Sahgal A, Stanisz GJ. Quantitative magnetization transfer in monitoring glioblastoma (GBM) response to therapy. *Sci Rep*. 2018;8(1):2475. doi:10.1038/s41598-018-20624-6
42. Mehrabian H, Myrehaug S, Soliman H, Sahgal A, Stanisz GJ. Evaluation of glioblastoma response to therapy with chemical exchange saturation transfer. *Int J Radiat Oncol*. 2018;101(3):713-723. doi:10.1016/j.ijrobp.2018.03.057
43. Jiang S, Eberhart CG, Lim M, et al. Identifying recurrent malignant glioma after treatment using amide proton transfer-weighted MR imaging: a validation study with image-guided stereotactic biopsy. *Clin Cancer Res*. 2019;25(2):552-561. doi:10.1158/1078-0432.CCR-18-1233
44. Park KJ, Kim HS, Park JE, Shim WH, Kim SJ, Smith SA. Added value of amide proton transfer imaging to conventional and perfusion MR imaging for evaluating the treatment response of newly diagnosed glioblastoma. *Eur Radiol*. 2016;26(12):4390-4403. doi:10.1007/s00330-016-4261-2
45. Choi YS, Ahn SS, Lee SK, et al. Amide proton transfer imaging to discriminate between low- and high-grade gliomas: added value to apparent diffusion coefficient and relative cerebral blood volume. *Eur Radiol*. 2017;27(8):3181-3189. doi:10.1007/s00330-017-4732-0
46. Regnery S, Adeberg S, Dreher C, et al. Chemical exchange saturation transfer MRI serves as predictor of early progression in glioblastoma patients. *Oncotarget*. 2018;9(47):28772-28783. doi:10.18632/oncotarget.25594
47. Sagiyama K, Mashimo T, Togao O, et al. In vivo chemical exchange saturation transfer imaging allows early detection of a therapeutic response in glioblastoma. *Proc Natl Acad Sci*. 2014;111(12):4542-4547. doi:10.1073/pnas.1323855111
48. Allen M, Bjerke M, Edlund H, Nelander S, Westermark B. Origin of the U87MG glioma cell line: good news and bad news. *Sci Transl Med*. 2016;8(354):354re3. doi:10.1126/scitranslmed.aaf6853
49. Saito R, Bringas JR, Panner A, et al. Convection-enhanced delivery of tumor necrosis Factor-related apoptosis-inducing ligand with systemic administration of temozolomide prolongs survival in an intracranial glioblastoma xenograft model. *Cancer Res*. 2004;64(19):6858-6862. doi:10.1158/0008-5472.CAN-04-1683
50. Haase A, Frahm J, Matthaei D, Hanicke W, Merboldt KD. FLASH imaging. Rapid NMR imaging using low flip-angle pulses. *J Comput Assist Tomogr*. 1986;10(2):363-368. doi:10.1016/0022-2364(86)90433-6
51. Rydberg JN, Riederer SJ, Rydberg CH, Jack CR. Contrast optimization of fluid-attenuated inversion recovery (FLAIR) imaging. *Magn Reson Med*. 1995;34(6):868-877. doi:10.1002/mrm.1910340612
52. Hennig J, Nauwerth A, Friedburg H. RARE imaging: a fast imaging method for clinical MR. *Magn Reson Med*. 1986;3(6):823-833. doi:10.1002/mrm.1910030602
53. Kim M, Gillen J, Landman BA, Zhou J, van Zijl PCM. Water saturation shift referencing (WASSR) for chemical exchange saturation transfer (CEST) experiments. *Magn Reson Med*. 2009;61(6):1441-1450. doi:10.1002/mrm.21873
54. Carr HY, Purcell EM. Effects of diffusion on free precession in nuclear magnetic resonance experiments. *Phys Rev*. 1954;94(3):630-638. doi:10.1103/PhysRev.94.630
55. Meiboom S, Gill D. Modified spin echo method for measuring nuclear relaxation times. *Rev Sci Instrum*. 1958;29(8):688-691. doi:10.1063/1.1716296
56. Basser PJ, Mattiello J, LeBihan D. Estimation of the effective self-diffusion tensor from the NMR spin echo. *J Magn Reson B*. 1994;103(3):247-254. doi:10.1006/jmrb.1994.1037
57. Pierpaoli C, Basser PJ. Toward a quantitative assessment of diffusion anisotropy. *Magn Reson Med*. 1996;36(6):893-906. doi:10.1002/mrm.1910360612
58. Strzeminska I, Factor C, Robert P, et al. Long-term evaluation of gadolinium retention in rat brain after single injection of a clinically relevant dose of gadolinium-based contrast agents. *Invest Radiol*. 2020;55(3):138-143. doi:10.1097/RLI.0000000000000623
59. Lee SH, Ban W, Shih YY. BrkRaw: a comprehensive tool to access raw Bruker Biospin MRI data. Published online June 2020. 10.5281/zenodo.3907018
60. Jenkinson M, Smith S. A global optimisation method for robust affine registration of brain images. *Med Image Anal*. 2001;5(2):143-156. doi:10.1016/S1361-8415(01)00036-6
61. Jenkinson M, Bannister P, Brady M, Smith S. Improved optimization for the robust and accurate linear registration and motion correction of brain images. *Neuroimage*. 2002;17(2):825-841. doi:10.1006/nimg.2002.1132
62. Guivel-Scharen V, Sinnwell T, Wolff SD, Balaban RS. Detection of proton chemical exchange between metabolites and water in biological tissues. *J Magn Reson*. 1998;133(1):36-45. doi:10.1006/jmre.1998.1440
63. Morrison C, Henkelman RM. A model for magnetization transfer in tissues. *Magn Reson Med*. 1995;33(4):475-482. doi:10.1002/mrm.1910330404
64. Windschuh J, Zaiss M, Meissner JE, et al. Correction of B1-inhomogeneities for relaxation-compensated CEST imaging at 7T. *NMR Biomed*. 2015;28(5):529-537. doi:10.1002/nbm.3283
65. R Core Team. R: a language and environment for statistical computing. Published online 2023. <https://www.R-project.org/>

66. Heo HY, Jones CK, Hua J, et al. Whole-brain amide proton transfer (APT) and nuclear Overhauser enhancement (NOE) imaging in glioma patients using low-power steady-state pulsed chemical exchange saturation transfer (CEST) imaging at 7T. *J Magn Reson Imaging*. 2016;44(1):41-50. doi:10.1002/jmri.25108
67. Dreher C, Oberhollenzer J, Meissner JE, et al. Chemical exchange saturation transfer (CEST) signal intensity at 7T MRI of WHO IV^o gliomas is dependent on the anatomic location. *J Magn Reson Imaging*. 2019;49(3):777-785. doi:10.1002/jmri.26215
68. Zhou J, Zaiss M, Knutsson L, et al. Review and consensus recommendations on clinical APT-weighted imaging approaches at 3T: application to brain tumors. *Magn Reson Med*. 2022;88(2):546-574. doi:10.1002/mrm.29241
69. Stanisz GJ, Odobrina EE, Pun J, et al. T₁, T₂ relaxation and magnetization transfer in tissue at 3T. *Magn Reson Med*. 2005;54(3):507-512. doi:10.1002/mrm.20605
70. Walsh JJ, Parent M, Akif A, et al. Imaging hallmarks of the tumor microenvironment in glioblastoma progression. *Front Oncol*. 2021;11:692650. doi:10.3389/fonc.2021.692650
71. Lenting K, Verhaak R, Ter Laan M, Wesseling P, Leenders W. Glioma: experimental models and reality. *Acta Neuropathol (Berl)*. 2017;133(2):263-282. doi:10.1007/s00401-017-1671-4
72. Qiang L, Yang Y, Ma YJ, et al. Isolation and characterization of cancer stem like cells in human glioblastoma cell lines. *Cancer Lett*. 2009;279(1):13-21. doi:10.1016/j.canlet.2009.01.016
73. Patil V, Pal J, Somasundaram K. Elucidating the cancer-specific genetic alteration spectrum of glioblastoma derived cell lines from whole exome and RNA sequencing. *Oncotarget*. 2015;6(41):43452-43471. doi:10.18632/oncotarget.6171
74. Sesen J, Dahan P, Scotland SJ, et al. Metformin inhibits growth of human glioblastoma cells and enhances therapeutic response. *PLoS ONE*. 2015; 10(4):e0123721. doi:10.1371/journal.pone.0123721
75. Akbarnejad Z, Eskandary H, Dini L, et al. Cytotoxicity of temozolomide on human glioblastoma cells is enhanced by the concomitant exposure to an extremely low-frequency electromagnetic field (100 Hz, 100 G). *Biomed Pharmacother*. 2017;92:254-264. doi:10.1016/j.biopha.2017.05.050
76. Bradley JD, Kataoka Y, Advani S, et al. Ionizing radiation improves survival in mice bearing intracranial high-grade gliomas injected with genetically modified herpes simplex Virus1. *Clin Cancer Res*. 1999;5(6):1517-1522.
77. Radaelli E, Ceruti R, Patton V, et al. Immunohistopathological and neuroimaging characterization of murine orthotopic xenograft models of glioblastoma multiforme recapitulating the most salient features of human disease. *Histol Histopathol*. 2009;24(7):879-891. doi:10.14670/HH-24.879
78. de Vries NA, Beijnen JH, van Tellingen O. High-grade glioma mouse models and their applicability for preclinical testing. *Cancer Treat Rev*. 2009;35(8): 714-723. doi:10.1016/j.ctrv.2009.08.011
79. Yao Z, Jiang X, Yao H, et al. Efficiently targeted therapy of glioblastoma xenograft via multifunctional biomimetic nanodrugs. *Biomater Res*. 2022;26(1): 71. doi:10.1186/s40824-022-00309-y
80. Wang H, Pan J, Yu L, Meng L, Liu Y, Chen X. MicroRNA-16 inhibits glioblastoma growth in orthotopic model by targeting cyclin D1 and WIP1. *OncoTargets Ther*. 2020;13:10807-10816. doi:10.2147/OTT.S250369
81. Gherardini L, Vetri Buratti V, Maturi M, et al. Loco-regional treatment with temozolomide-loaded thermogels prevents glioblastoma recurrences in orthotopic human xenograft models. *Sci Rep*. 2023;13(1):4630. doi:10.1038/s41598-023-31811-5
82. Senrunga A, Tripathi T, Yadav J, et al. In vivo antiangiogenic effect of nimbolide, trans-chalcone and piperine for use against glioblastoma. *BMC Cancer*. 2023;23(1):1173. doi:10.1186/s12885-023-11625-4

SUPPORTING INFORMATION

Additional supporting information can be found online in the Supporting Information section at the end of this article.

How to cite this article: Lam WW, Chudzik A, Lehman N, et al. Saturation transfer (CEST and MT) MRI for characterization of U-87 MG glioma in the rat. *NMR in Biomedicine*. 2025;38(1):e5282. doi:10.1002/nbm.5282